Final Report

K. R. Chu   August 28, 2010

REF: AOARD FA2386-09-1-4099

Project Name: Research on Novel High-Power Microwave/Millimeter Wave Sources and Applications

Principal Investigator: K. R. Chu, Department of Physics, National Tsing Hua University, Hsinchu, Taiwan; Email: krchu@phys.nthu.edu.tw; Tel: 886-3-571-0712

Co- Principal Investigator: N. C. Luhamnn, Jr., Department of Applied Science, University of California, Davis, CA, 95616, nalumann@usdavis.edu, Tel. 530-752-5414

Period of Performance: June 1, 2009 – May 31, 2010

Attachments: Publication 1. L. R. Barnett, N. C. Luhmann Jr., C. C. Chiu, and K. R. Chu, "Relativistic Performance Analysis of an Advanced High-Current-Density Magnetron Injection Gun," Phys. Plasmas 16, 093111 (2009).

Publication 2. C. C. Chiu, C. Y. Tsai, S. H. Kao and K. R. Chu, L. R. Barnett and N. C. Luhmann, Jr., "Study of a High-Order-Mode Gyrotron Traveling-Wave Amplifier," submitted to Phys. Plasmas.

In this project, our tasks are to provide theoretical support for the experiments at UC Davis aimed at the development of a zero-drive stable W-band gyrotron traveling-wave amplifier (Gyro-TWT). The first of these tasks is the development of a fully relativistic theory for the interpretation of the test results of the most critical component of this gyro-TWT; namely, a new type of electron gun based on the robust, long-lived, clean, low work function, high current density thermionic cathodes recently developed at UC Davis under the sponsorship of MURI-04. This is an electron gun to be used for the zero-drive stable Gyro-TWT.

Our second task concerns the design of a novel W-band gyro-TWT, which is to yield over 100 kW with 5% bandwidth and 70 dB gain. The bandwidth is sufficiently wide for the generation of appropriately chirped pulses with pulse compression. Hence, it is suited for the ongoing upgrading of high-resolution space radars operated by Lincoln Laboratory, for which an array of 1%-bandwidth sources is being planned due to the lack of a broadband source.

Report Documentation Page		*Form Approved* *OMB No. 0704-0188*

Public reporting burden for the collection of information is estimated to average 1 hour per response, including the time for reviewing instructions, searching existing data sources, gathering and maintaining the data needed, and completing and reviewing the collection of information. Send comments regarding this burden estimate or any other aspect of this collection of information, including suggestions for reducing this burden, to Washington Headquarters Services, Directorate for Information Operations and Reports, 1215 Jefferson Davis Highway, Suite 1204, Arlington VA 22202-4302. Respondents should be aware that notwithstanding any other provision of law, no person shall be subject to a penalty for failing to comply with a collection of information if it does not display a currently valid OMB control number.

1. REPORT DATE **31 AUG 2010**	2. REPORT TYPE **FInal**	3. DATES COVERED **01-06-2009 to 31-05-2010**
4. TITLE AND SUBTITLE **Research on Novel High-Power Microwave/Millimeter Wave Sources and Applications**		5a. CONTRACT NUMBER **FA23860914099**
		5b. GRANT NUMBER
		5c. PROGRAM ELEMENT NUMBER
6. AUTHOR(S) **Kwo Ray Chu**		5d. PROJECT NUMBER
		5e. TASK NUMBER
		5f. WORK UNIT NUMBER
7. PERFORMING ORGANIZATION NAME(S) AND ADDRESS(ES) **National Tsing Hua University,Kuang 3-572-1142,Hsinchu 300,Taiwan,TW,300**		8. PERFORMING ORGANIZATION REPORT NUMBER **N/A**
9. SPONSORING/MONITORING AGENCY NAME(S) AND ADDRESS(ES) **AOARD, UNIT 45002, APO, AP, 96337-5002**		10. SPONSOR/MONITOR'S ACRONYM(S) **AOARD**
		11. SPONSOR/MONITOR'S REPORT NUMBER(S) **AOARD-094099**

12. DISTRIBUTION/AVAILABILITY STATEMENT **Approved for public release; distribution unlimited**

13. SUPPLEMENTARY NOTES

14. ABSTRACT

In this project, theoretical support was provided for the experiments at UC Davis aimed at the development of a zero-drive stable W-band gyrotron traveling-wave amplifier (Gyro-TWT). The first of these tasks is the development of a fully relativistic theory for the interpretation of the test results of the most critical component of this gyro-TWT; namely, a new type of electron gun based on the robust, long-lived, clean, low work function, high current density thermionic cathodes recently developed at UC Davis under the sponsorship of MURI-04. This is an electron gun to be used for the zero-drive stable Gyro-TWT. The second task was to design a novel W-band gyro-TWT, to yield over 100 kW with 5% bandwidth and 70 dB gain. The bandwidth is sufficiently wide for the generation of appropriately chirped pulses with pulse compression. Hence, it is suited for the ongoing upgrading of high-resolution space radars operated by Lincoln Laboratory, for which an array of 1%-bandwidth sources is being planned due to the lack of a broadband source.

15. SUBJECT TERMS

microwave devices, microwave sources

16. SECURITY CLASSIFICATION OF:			17. LIMITATION OF ABSTRACT	18. NUMBER OF PAGES	19a. NAME OF RESPONSIBLE PERSON
a. REPORT **unclassified**	b. ABSTRACT **unclassified**	c. THIS PAGE **unclassified**	**Same as Report (SAR)**	**28**	

Under the support of this contract, Co-PI Prof. Luhamann paid a visit to National Tsing Hua University in June, 2009 and PI Prof. Chu paid a return visit to UC Davis in March, 2010. As a result of the close interaction, we have completed both tasks and two papers have come out this collaboration. In both papers, the sponsorship of AFOSR/AOARD has been acknowledged. The first paper has already been published [L. R. Barnett, N. C. Luhmann Jr., C. C. Chiu, and K. R. Chu, "Relativistic Performance Analysis of an Advanced High-Current-Density Magnetron Injection Gun," Phys. Plasmas 16, 093111 (2009)]. The full paper is an attachment to this report. Here, we quote the abstract of this publication:

"Electron beam quality is essential to the performance of millimetre-wave gyro-amplifiers, particularly the gyrotron traveling-wave amplifier (gyro-TWT) which is extremely sensitive to the electron velocity spread and emission uniformity. As one moves up in power and frequency, the quality of the electron beam becomes even more critical. One aspect of the electron beam formation technology which has received relatively little attention has been the performance analysis of the electron beam itself. In this study, a 100 kV, 8 A magnetron injection gun (MIG) with a calculated perpendicular-to-parallel velocity ratio of 1.4 and axial velocity spread of 3.5% has been designed, tested, and analyzed. It is shown that the equipment precision and a fully relativistic data analysis model afford sufficient resolution to allow a verification of the theoretical predictions as well as a quantitative inference to the surface roughness of the cathode used."

We believe that this paper has established a milestone in electron beam formation technology employing the magnetron injection gun. In this work, a high emission current density (30 A/cm^2) 94 GHz MIG using state-of-the-art scandate impregnated type commercial cathodes has been tested with a newly developed axial energy beam analyzer. As a significant progress in MIG diagnostics, precision machining and relativistic data analysis allow an accurate quantitative comparison between calculated and measured beam performance. As a result, it is possible to resolve the effects of cathode surface roughness (and possibly other defects) on the beam axial energy spread, from which the cathode surface quality can be inferred. For the present 94 GHz MIG, the inferred cathode surface roughness (particle radius) is ~1.1 µm, which introduces an additional velocity spread of 1.1% on top of the 3.5% due to electron optics. This is tolerable for the present MIG, but the need for nanocomposite cathodes is clearly seen for higher frequencies.

The second paper has just been submitted to the Physics of Plasmas for publication [C. C. Chiu, C. Y. Tsai, S. H. Kao and K. R. Chu, L. R. Barnett and N. C. Luhmann, Jr., "Study of a High-Order-Mode Gyrotron Traveling-Wave Amplifier".] The full manuscript is an attachment to this report. Here we quote the abstract:

"Performance characteristics of a fundamental cyclotron harmonic, TE_{01}-mode gyrotron traveling-wave amplifier are studied theoretically under the marginal stability condition. Absolute instabilities on both lower and higher order modes at the fundamental and second cyclotron harmonic frequencies present severe constraints to the stable operating current and hence the device capability. General methods for stabilizing these unwanted oscillations are outlined, on the basis of which the gain, power, bandwidth, and efficiency are examined in a multi-dimensional parameter space under the marginal stability criterion. The results provide a basis for tradeoff considerations among power, bandwidth, and efficiency to reach an optimized design with the desired features. General trends are discussed and specific design examples, all with an ultra high gain, are presented as illustrative examples.
"

In this paper, we have investigated the design tradeoffs of a high-order-mode, distributed-loss gyro-TWT on the basis of the marginal stability criterion. The beam current of the gyro-TWT is mainly constrained by large-k_z, TE_{11} absolute instability while the low-k_z absolute instabilities limit the copper section length. Simulation results show that a low beam velocity ratio is suitable for high power and broadband designs, while a high beam velocity ratio is suitable for high efficiency operation. Heavy wall resistivity enables high current and high power operation, while also increasing the wall loading of the circuit. Simulation results show that a long lossy section can always be employed for ultra high gain, with a minimum effect on the bandwidth and a moderate reduction in output power and efficiency. In summary, the parametric dependence and tradeoff considerations presented in this study provide a useful design guideline for high performance, stably operated gyro-TWTs.

Relativistic performance analysis of a high current density magnetron injection gun

L. R. Barnett,[1] N. C. Luhmann, Jr.,[1] C. C. Chiu,[2] and K. R. Chu[2]
[1]*Department of Applied Science, University of California-Davis, Davis, California 95616, USA*
[2]*Department of Physics, National Tsing Hua University, Hsinchu 300, Taiwan*

Electron beam quality is essential to the performance of millimeter-wave gyroamplifiers, particularly the gyrotron traveling-wave tube amplifier, which is extremely sensitive to the electron velocity spread and emission uniformity. As one moves up in power and frequency, the quality of the electron beam becomes even more critical. One aspect of the electron beam formation technology which has received relatively little attention has been the performance analysis of the electron beam itself. In this study, a 100 kV, 8 A magnetron injection gun with a calculated perpendicular-to-parallel velocity ratio of 1.4 and axial velocity spread of 3.5% has been designed, tested, and analyzed. It is shown that the equipment precision and a fully relativistic data analysis model afford sufficient resolution to allow a verification of the theoretical predictions as well as a quantitative inference to the surface roughness of the cathode used. © *2009 American Institute of Physics*. [doi:10.1063/1.3227649]

I. INTRODUCTION

In the magnetron injection gun (MIG),[1,2] electrons from an annular emitter are accelerated at an angle to the external magnetic field and perform helical orbits. The MIG has been successfully employed in gyrodevices since its first use in the 1960s.[3,4] However, when one extends the operation of these devices to the *W*-band (75–110 GHz) and beyond, critical thermionic cathode issues begin to emerge. We first note that, while gyrotron traveling-wave tubes (gyro-TWTs) have been made to work well at lower frequencies (e.g., 35 GHz) in good agreement with theoretical predictions,[5] the 94 GHz, 140 kW, 60 dB gyro-TWT developed at the University of California at Davis (UCD) has achieved a bandwidth of only 2.4%.[6] This narrow bandwidth can be traced directly to poor electron beam quality and, in particular, the electron velocity spread. Part of this spread has been found to be due to geometrical and focusing effects in the as-fabricated MIG, but estimates of other contributions due to cathode surface roughness, temperature, machining errors, and misalignment errors are also very large. In addition to these typical problems, Anderson *et al.*[7] have reported large local (microscopic scale) work function variations leading to emission nonuniformities with large areas that do not or very poorly emit, resulting in increased velocity spread. In addition, cathode nonuniformity itself also lowers the interaction efficiency.[8]

If a device is scaled from a lower frequency to a higher frequency (e.g., 35–95 GHz), then to obtain comparable performance all dimensions need to be scaled proportional to wavelength, including errors and cathode roughness. Closer machining tolerances and alignment tolerances may be difficult, but can be accomplished. A more difficult requirement is that of obtaining a factor of 3 (or better) cathode surface smoothness. A standard commercial cathode is made from tungsten powder that has an average diameter of about 5 μm, although the variation in particle size is large, ranging from submicron particles to particles of tens of microns. The cathodes are generally cut on a lathe to be as smooth as possible; however, grinding is generally avoided because it closes the pores and introduces foreign materials into the pores. It is common to visibly observe small cutting grooves on a cathode surface indicating a machined roughness of tens of microns.[9]

Furthermore, as a cathode ages, its surface becomes eroded (possibly from ion bombardment and sputtering) and the larger particles become dominant on the surface. Thus, while a new cathode can appear smooth and shiny, one that has aged in a working tube at the relatively high temperature of ~1180 °C is no longer smooth and shiny. The appearance under an optical microscope can be roughness on the order of tens of microns. Applying such roughness, calculations show that cathode roughness is a significant limitation to gyro-TWTs at 94 GHz and above.

To scale upward in frequency, not only should the cathode roughness be scaled proportional to wavelength, but the cathode dimensions as well. This means that to directly scale a successful 10 A/cm^2 gun design from 35 to 95 GHz, then the 95 GHz cathode would have to operate at a current density of 74 A/cm^2! Since this is impossible with presently available commercial cathodes, one must use a proportionally larger magnetic field compression ratio in order to accommodate the current density limitation. This is extremely detrimental as the spread from all cathode errors are magnified greatly by the compression ratio. While assessing the precise degree of worsening due to all factors is a very complex problem involving three-dimensional analysis of the many factors, it is estimated that an order of magnitude of increase in velocity spread could result. At a minimum, we can expect significantly worse performance in a 94 GHz MIG than a 35 GHz MIG with both operating at the same emission density with similar cathodes and errors.

As discussed above, a new generation of cathodes with unprecedented current density and surface smoothness will

16, 093111-1

TABLE I. Predicted and measured MIG parameters.

	EGUN prediction (smooth cathode)	Measurement
Voltage (kV)	100.0	100.0
Current (A)	8.0	8.0
α_0	1.40	1.40
$\Delta v_z / v_{z0}$	3.5%	4.6%

be required for the development of future gyroamplifiers aimed at much higher power and/or frequency. Significant progress has been made at UCD in the development of tungsten-scandate nanopowder based cathodes.[10] Concurrently, we have set up a precision facility for beam testing and developed a relativistic theory for the interpretation of the test data. Our focus of this paper is the demonstration and analysis of an advanced high-current MIG based on the best available commercially available cathode. In Sec. II, we outline the design features and significance of the new MIG. In Sec. III, a novel axial energy beam analyzer is described together with the test data. In Sec. IV, this is followed by the development of a theoretical model, which reduces the test data into velocity and pitch angle spreads. Finally, in Sec. V, we draw conclusions from the present study and discuss the prospects for next-phase MIGs based on the nanopowder cathode technology.

II. DESIGN FEATURES OF A HIGH CURRENT DENSITY MIG

In the design of a high current density *W*-band MIG, we have taken a number of measures to improve the beam quality. The magnetic compression ratio has been reduced from the previous value of 35 (Ref. 6) to approximately 12. The cathode magnetic field is 3.0 kG and the final magnetic field is 35.6 kG. This considerably reduces possible errors from misalignments that result in beam quality degradation. The low compression ratio requires a smaller cathode surface area, and consequently an emission density approximately three times higher than the conventional limit of 10 A/cm². For this reason, we have utilized the state-of-the-art Spectra-Mat 612X scandate cathode material to obtain high current density with acceptable operating temperature and lifetime.

The MIG is optimized with the EGUN code for a cathode voltage (V_b) of 100 kV and a beam current (I_b) of 8 A (corresponding to a cathode current density of 30 A/cm²). The accelerating electric field has been increased from the standard cw maximum of ~100 kV/cm to 205 kV/cm, which is tolerable for pulsed operations. Neglecting the contributions due to cathode surface roughness, emission non-uniformity, and other defects, the calculated velocity ratio $\alpha_0 (= v_{\perp 0}/v_{z0})$ is 1.40 with an axial velocity spread ($\Delta v_z/v_{z0}$) of 3.5%, where $v_{\perp 0}$ and v_{z0} are, respectively, the mean values of perpendicular and parallel velocities, and Δv_z is the standard deviation of the axial velocity from v_{z0}. The corresponding perpendicular velocity spread is 1.79%. The final design parameters are summarized in column 2 of Table I.
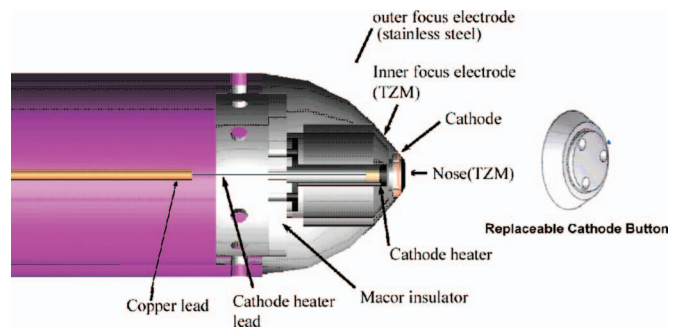

FIG. 1. (Color) The cathode assembly. The replaceable cathode button is shown on the right.

An MIG with a velocity spread of 3%–5% has been routinely achieved in MIG simulations, but rarely measured in a direct manner partly because the mainstream gyromonotrons used for plasma heating are insensitive to the velocity spread. Our purpose here is to experimentally analyze a low velocity spread MIG and thereby benchmark the design code and theory, which can be of considerable importance to the development of other types of gyrotrons.

In order to carry out cathode and MIG beam quality studies, an approach was adopted for mounting and heating cathodes that also solves alignment, heater, and gap problems, permits changing focusing electrodes, and allows very high heating power to be used to investigate a wide variety of cathodes that only need to be made in a button form, and made very quickly and cheaply, as there needs to be no mounting brackets, heat shields or heaters attached (see Fig. 1). Note that there are no gaps to perturb the beam, and no long thin supports to cause misalignment. It is sandwiched together with pins, self-aligning, and e-beam heated with a 2 keV electron gun for high temperature. The thermal contact of such parts is very low and essentially all heating is via radiation, and consequently the Mo/TZM parts should run below emission temperature. For additional safety, the Mo parts are carburized for further emission suppression.

Figure 2 is an EGUN drawing of the MIG configuration/dimensions and electron trajectories. The design is flexible
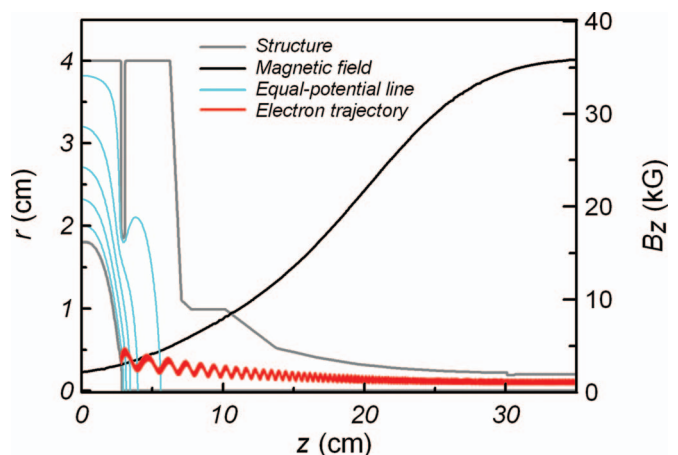

FIG. 2. (Color) EGUN drawing of the overall MIG configuration/dimensions and electron trajectories.
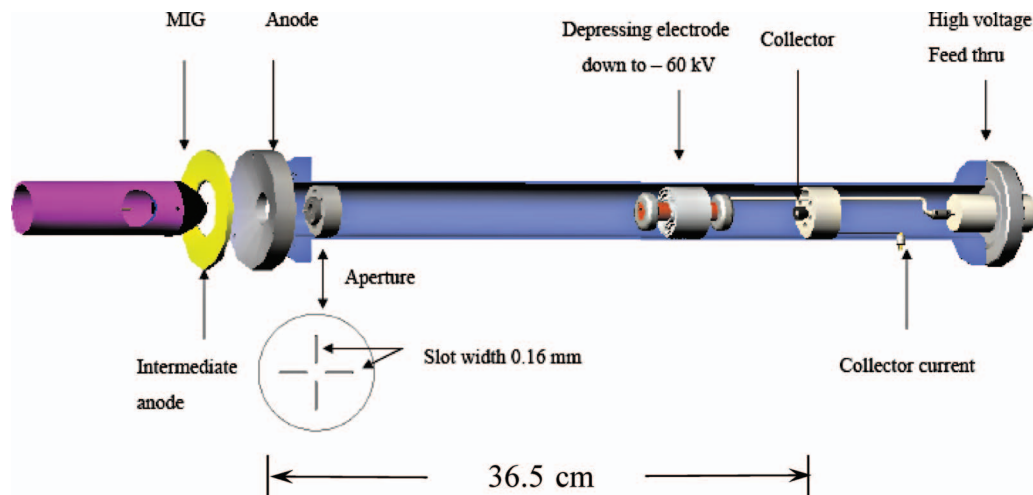
FIG. 3. (Color) Schematic of the MIG and axial energy beam analyzer.

with respect to maintaining the beam quality with variable operating parameters such as voltage, current, and magnetic compression ratio.

III. BEAM ANALYZER AND MIG TEST RESULTS

MIG diagnostics have not been so frequently reported in literature. Some of the work has focused on the cathode emission nonuniformity, where typically a mechanically rotatable current probe has been employed.[1,7] A model has also been developed to identify the source of emission nonuniformity.[11]

The group at the Institute of Applied Physics (IAP), Russia, has measured the electron energy spectrum from the current passing through a decelerating grid placed away from an exit on the side wall of the collector.[12] The IAP group has also measured both the electron velocity spread and cathode emission nonuniformity by using diaphragms and a decelerating net placed directly in the interaction region.[13]

Diagnostics has also been conducted on an axis-encircling electron beam produced by passing a linear electron beam through a magnetic cusp. Jeon *et al.*[14] have measured the velocity ratio and axial velocity spread of this type of electron beam with a capacitive probe and a phosphor screen. Varying the cathode-cusp distance and beam and magnetic field parameters, they measured a minimum axial velocity spread of about 1.5% and the trend of the data agrees with EGUN calculations.

Here, we have designed and constructed an axial energy beam analyzer (Fig. 3) to measure the electron velocity spread of the MIG in the operating magnetic field, aimed at a quantitative comparison between predictions and measurements. The analyzer operates on the principle of a depressing electrode to reflect electrons of lower axial energy than the bias voltage of the electrode. The electrons of higher axial energy pass the depressing electrode with subsequent collection by a separate collector. The velocity distribution can then be calculated from this measurement (Sec. IV).

To prevent the reflected electrons from returning to the MIG and altering the focusing dynamics, a sampling aperture is employed at the exit of the MIG. In this case, a crossed slot pattern (each 0.16 mm in width) is used to effectively take an average sample over four small sections of the beam. The collected current is monitored with a calibrated current transformer. For improved spatial resolution, a single small aperture could be used, and made moveable to scan the beam. Figure 4 shows a typical data scan of collector current I_{coll} versus the depressing electrode voltage V_{dep}.

IV. RELATIVISTIC ANALYSIS OF THE TEST DATA

In the beam analyzer, the electrons move in a uniform static magnetic field and a nonuniform static electric field due to the negative potential on the depressing electrode. The transverse motion of the electrons is oscillatory and restricted within a radial excursion of only two Larmor radii. Under such conditions, the axial electric field may significantly reduce the electron axial velocity (or γ), but the transverse electric field plays a negligible role. Thus, we may neglect the effects of the transverse electric field and assume the perpendicular momentum $p_\perp$ to be a constant of the motion. However, transverse and axial motions are relativistically coupled. For example, the constancy of the relativistic momentum $p_\perp(=\gamma m v_\perp)$ implies that $v_\perp$ increases with decreasing γ as an electron is decelerated in the axial electric field, whereas the constancy of the nonrelativistic $p_\perp(=m v_\perp)$
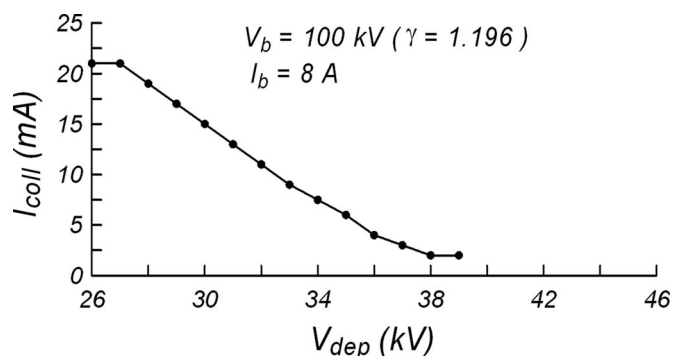

FIG. 4. Measured collector current I_{coll} vs the depressing electrode voltage V_{dep}. V_b=100 kV and I_b=8 A. Most of the electrons are intercepted by the sampling aperture.
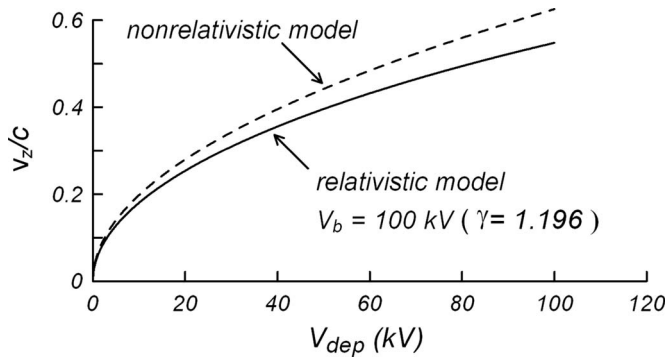
FIG. 5. Plot of v_z vs V_{dep} for $V_b = 100$ kV ($\gamma = 1.196$), where v_z gives the boundary value between reflecting and passing electrons at the corresponding V_{dep}. Solid and dashed curves are based on relativistic and nonrelativistic models, respectively.

FIG. 6. Upper figure: measured electron distribution in v_z. The average value (v_{z0}) and axial velocity spread ($\Delta v_z / v_{z0}$) are indicated in the figure. Lower figure: measured electron distribution in α with the average value (α_0) indicated in the figure. Both figures are based on the measured data in Fig. 3 and the relativistic plot in Fig. 4.

implies a constant $v_\perp$. As a result, the nonrelativistic model tends to underestimate the particle's α value. For a more accurate interpretation of the test data, it is therefore desirable to use a relativistic model.

The Lorentz factor of an electron can be written,

$$\gamma^2 = 1 + \frac{p_\perp^2}{m^2 c^2} + \frac{p_z^2}{m^2 c^2}, \tag{1}$$

where $p_\perp$ and p_z are, respectively, the momenta perpendicular and parallel to the z-axis. Then, if the depressing electrode is maintained at a voltage of V_{dep} and the electron axial velocity becomes exactly zero at the position of the depressing electrode, we have (by conservation of energy)

$$\left[\gamma - \frac{V_{dep}(\text{kV})}{511} \right]^2 = 1 + \frac{p_\perp^2}{m^2 c^2}, \tag{2}$$

where $p_\perp$ remains a constant by assumption.

Subtracting Eq. (2) from Eq. (1) gives

$$\gamma^2 - \left(\gamma - \frac{V_{dep}(\text{kV})}{511} \right)^2 = \frac{p_z^2}{m^2 c^2}. \tag{3}$$

Equation (3) is valid only when the electron with maximum p_z (or zero $p_\perp$) can reach the depressing electrode, i.e., when

$$\gamma - \frac{V_{dep}(\text{kV})}{511} \geq 1, \tag{4}$$

which sets a maximum value for V_{dep}.

Writing $p_z = \gamma m v_z$, we obtain from Eq. (3)

$$\frac{v_z}{c} = \frac{1}{\gamma} \left\{ \frac{V_{dep}(\text{kV})}{511} \left[2\gamma - \frac{V_{dep}(\text{kV})}{511} \right] \right\}^{1/2}, \tag{5}$$

subject to condition (4). Note that, here and below, v_z and γ refer to unperturbed values (i.e., values before the electrons enter the static electric field). Equation (5), plotted in a solid curve in Fig. 5, thus relates V_{dep} to the value of v_z, under which an electron will be reflected. In Fig. 5, the dashed curve represents the nonrelativistic relation between v_z and V_{dep} following a similar derivation. For reasons just discussed, it can be seen that there is a considerable difference between the relativistic and nonrelativistic models.
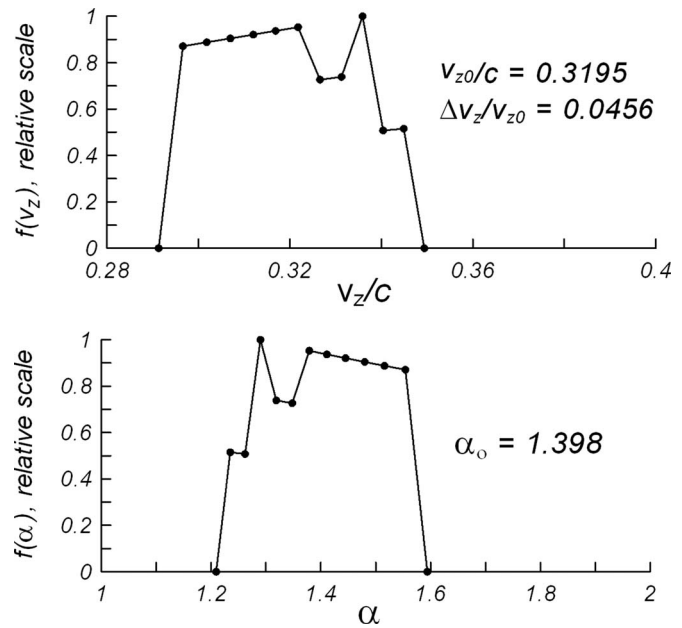
We assume that all electrons in the unperturbed beam have the same energy (γ), but with a spread in velocity ratio $\alpha(= v_\perp / v_z)$. Then, for a given γ, Eq. (5) gives the value of the unperturbed v_z which divides the reflecting electrons from the passing electrons at a given V_{dep}. Thus, through Eq. (5), the experimental data in terms of I_{coll} versus V_{dep} (see Fig. 4) can be reduced to a curve of I_{coll} versus v_z. From this curve, we may evaluate the differential quantity $\Delta I_{coll} / \Delta v_z$ as a function of v_z, which gives the measured electron distribution function in v_z [denoted by $f(v_z)$ in upper Fig. 6]. From $f(v_z)$, we may also obtain the electron distribution function in α [denoted by $f(\alpha)$ in lower Fig. 6].

Figure 6 shows a measured α_0 value of 1.40, in excellent agreement with the EGUN prediction (see Table I). On the other hand, the measured axial velocity spread of 4.6% is higher than the EGUN prediction of 3.5%. This difference can be attributed to the effects of cathode surface roughness shown in Fig. 7. Here, we first plot the predicted velocity spread (3.5%) from the EGUN code neglecting surface roughness. The contribution due to bumps is then estimated using a simple model in which the bump caused velocity spread is proportional to the square root of the particle radius.[1] If we assume that the additional spread over the EGUN predicted value is due to surface roughness, then Fig. 7 implies a surface roughness of ~ 1.1 μm for this new and very smoothly diamond cut cathode.

V. CONCLUSION AND DISCUSSION

A high emission current density (30 A/cm^2) 94 GHz MIG using state-of-the-art scandate impregnated type commercial cathodes has been tested with a newly developed axial energy beam analyzer. As a significant progress in MIG
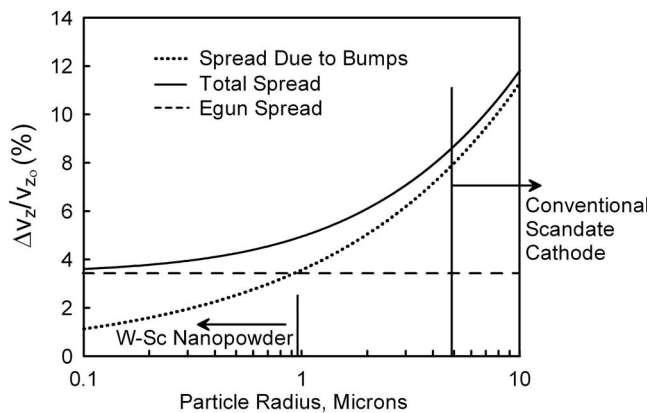
FIG. 7. Estimated dependence of axial velocity spread on cathode surface roughness.

diagnostics, precision machining and relativistic data analysis allow an accurate quantitative comparison between calculated and measured beam performance (Table I). As a result, it is possible to resolve the effects of cathode surface roughness (and possibly other defects) on the beam axial energy spread, from which the cathode surface quality can be inferred. For the present 94 GHz MIG, the inferred cathode surface roughness (particle radius) is ~1.1 μm, which introduces an additional velocity spread of 1.1% on top of the 3.5% due to electron optics. This is tolerable for the present MIG, but the need for nanocomposite cathodes is clearly seen for higher frequencies.

Such nanocomposite cathodes are being developed at UCD. The grain size in the UCD matrix is 500–700 nm and very uniform.[10] Scaling from Fig. 7, it is seen that this can significantly reduce the overall velocity spread of a MIG at frequencies well above 94 GHz, which will manifest itself as a substantial increase in, for example, the bandwidth for the gyro-TWT. In fact, because of its extreme sensitivity to the velocity spread,[15] the gyro-TWT itself serves as a valuable beam diagnostic tool as very small velocity spreads are achieved.

Another point to be stressed about the nanocomposite cathodes is that they provide considerably higher current density at lower temperatures than the best commercially available cathodes. The nanocomposite cathodes readily operate at 80 A/cm^2 at $T=1150$ °C$_b$ in fully space charge limited (SCL) operation,[10] in contrast to the best Spectra-mat 612X scandate cathode which provides only 30 A/cm^2 non-SCL at $T=1135$ °C$_b$. This together with its smoothness offers the possibility a dramatic advance in gyrodevices performance capability.

ACKNOWLEDGMENTS

[1]Sh. E. Tsimring, *Electron Beams and Microwave Vacuum Electronics* (Wiley, New York, 2006), Sec. 10-8.
[2]J. M. Baird and W. Lawson, Int. J. Electron. **61**, 953 (1986).
[3]A. V. Gaponov, A. L. Gol'denberg, D. P. Grigor'ev, I. M. Orlova, T. P. Pankratova, and M. I. Petelin, JETP Lett. **2**, 267 (1965).
[4]R. L. Schriever and C. C. Johnson, Proc. IEEE **54**, 2029 (1966).
[5]K. R. Chu, H. Y. Chen, C. L. Hung, T. H. Chang, L. R. Barnett, S. H. Chen, and T. T. Yang, Phys. Rev. Lett. **81**, 4760 (1998).
[6]H. H. Song, D. B. McDermott, Y. Hirata, L. R. Barnett, C. W. Domier, H. L. Hsu, T. H. Chang, W. C. Tsai, K. R. Chu, and N. C. Luhmann, Jr., Phys. Plasmas **11**, 2935 (2004).
[7]J. P. Anderson, S. E. Korbly, R. J. Temkin, M. A. Shapiro, K. L. Felch, and S. Cauffman, IEEE Trans. Plasma Sci. **30**, 2117 (2002).
[8]G. S. Nusinovich, A. N. Vlasov, M. Botton, T. M. Antonsen, Jr., S. Cauffman, and K. Felch, Phys. Plasmas **8**, 3473 (2001).
[9]S. Chen, D. Head, M. Effgen, and I. S. Jawahir, IEEE Trans. Electron Devices **52**, 903 (2005).
[10]J. Zhao, N. Li, J. Li, and N. C. Luhmann, Jr., *Proceedings of the IEEE International Vacuum Electronics Conference*, Rome, Italy, 2009, edited by Technical Programme Committee (IEEE, New York, 2009), p. 523.
[11]K. L. Jensen, Y. Y. Lau, and N. Jordan, Appl. Phys. Lett. **88**, 164105 (2006).
[12]N. P. Venediktov, M. Yu. Glyavin, A. L. Goldenberg, V. E. Zapevalov, A. N. Kuftin, and A. S. Postnikova, Tech. Phys. **45**, 476 (2000) [translated from Zh. Tekh. Fiz. **70**, 95 (2000)].
[13]M. Yu. Glyavin, A. L. Goldenberg, A. N. Kuftin, V. K. Lygin, A. S. Postnikova, and V. E. Zapevalov, IEEE Trans. Plasma Sci. **27**, 474 (1999).
[14]S. G. Jeon, C. W. Baik, D. H. Kim, G. S. Park, N. Sato, and K. Yokoo, Appl. Phys. Lett. **84**, 1994 (2004).
[15]See, for example, K. R. Chu, H. Guo, and V. L. Granatstein, Phys. Rev. Lett. **78**, 4661 (1997).

Study of a High-Order-Mode Gyrotron Traveling-Wave Amplifier

C. C. Chiu, C. Y. Tsai, and S. H. Kao

Department of Physics, National Tsing Hua University, Hsinchu, Taiwan

K. R. Chu

Department of Physics, National Taiwan University, Taipei, Taiwan

L. R. Barnett and N. C. Luhmann, Jr.

Department of Applied Science, University of California, Davis, CA 95616

Abstract

Performance characteristics of a fundamental cyclotron harmonic, distributed-loss, TE_{01}-mode gyrotron traveling-wave amplifier are studied theoretically. Absolute instabilities on both lower and higher order modes at the fundamental and second cyclotron harmonic frequencies present a severe limitation to the stable operating current and hence the device capability. General methods for stabilizing these unwanted oscillations are outlined, on the basis of which the gain, power, bandwidth, and efficiency are examined in a multi-dimensional parameter space under the marginal stability criterion. The results provide a basis for tradeoff considerations among power, bandwidth, and efficiency to reach a stable design optimized for the desired features. General trends are discussed and specific design examples, all with an ultra high gain, are presented as illustrative examples.

I. INTRODUCTION

In contrast to conventional linear beam devices, gyro-devices based on the electron cyclotron maser instability [1-6] employ a smooth and larger-size fast-wave circuit for high power operation. Furthermore, gyrating electrons can resonantly interact with a high-order mode at the fundamental or a higher cyclotron harmonic frequency by means of magnetic field adjustment to match the beam-wave synchronism condition

$$\omega - k_z v_z - s\Omega_c \approx 0 \tag{1}$$

where ω is the wave frequency, k_z is the propagation constant, v_z is the electron axial velocity, s is the cyclotron harmonic number, and Ω_c is the relativistic electron cyclotron frequency. Thus, by providing an extra degree of freedom, the intrinsic cyclotron frequency allows gyro-devices to operate in an over-moded circuit with even greater power handling capability.

There are two basic types of gyro-amplifiers: the gyroklystron amplifier and the gyrotron traveling-wave amplifier (gyro-TWT). The gyroklystron amplifier [7-9] produces significantly higher powers than available from conventional slow-wave devices. A state-of-the-art gyroklystron has been employed in a transportable, W-band advanced radar named WARLOC for imaging, scientific and cloud physics studies [10]. The bandwidth of gyroklystrons, limited by the Q-value of the cavities, is typically below 1%. The gyro-TWT [11-18], on the other hand, features a much broader instantaneous bandwidth, which is capable of meeting the critical need for pulse chirping and compression in high-resolution radar applications. For this reason, a W-band gyro-TWT has been developed as a broadband driver for the upgrade of long-range radar systems [19-21].

The non-resonant interaction circuit (essentially a waveguide structure), which gives the gyro-TWT the broadband advantage, also makes it susceptible to absolute instabilities. In an absolute instability, the electron beam amplifies a backward wave, which travels upstream to reinforce the bunching action on the incoming electron beam. Self oscillations thus result from an internal feedback loop. The absolute instability occurs only at a discrete set of frequencies determined by the phase coherence within the internal feedback loop [22]. Hence, it is not a common phenomenon in a cavity-based gyro-device, which has a different set of resonant frequencies. However, for the gyro-TWT, it presents a serious problem even in the lowest order (TE$_{11}$) mode operation [23]. For a high-order mode gyro-TWT, the performance is much more severely constrained by the absolute instabilities [18]. Considerable progress has been made in recent years on the suppression of the absolute instability [12, 14] and a general recipe is provided in Ref. 24.

According to this recipe [24], zero-drive stability can be achieved in two stages: a heavily lossy linear section to eliminate the most persistent absolute instabilities and a shortened nonlinear (copper) section to suppress the remaining ones. A proper combination of these two

methods can thus be used to realize stable designs with different desired features. Such a scheme is examined in the current paper. Ideally, an optimized design is one that operates just below the threshold of the first absolute instability. Thus, we adopt the "marginal stability" criterion as a design guideline. In reality, unmodelled effects, such as end reflections [25, 26], can significantly reduce the predicted performance. Nevertheless, marginally stable designs provide a useful reference for an estimate the ultimate performance as well as a basis for trade-off considerations.

We have examined the TE_{01}-mode, distributed-loss gyro-TWT in a broad parameter space under the marginal stability criterion. Optimum regimes are identified, which provide the basis for design tradeoffs among gain, power, efficiency, and bandwidth. The gyro-TWT model is described in Sec. II. In Sec. III, we review the characteristics of different absolute instabilities and outline methods for their suppression. In Sec. IV, zero-drive stable gyro-TWT performance is examined in a vast parameter space and design tradeoffs are considered. From the results, we discuss the general trends observed along with illustrative design examples. Finally, conclusions are drawn in Sec. IV.

II. MODEL

The TE_{01} mode gyro-TWT under study is composed of a lossy linear section followed by a copper nonlinear section (Fig. 1). Both sections are of the same radius. A single-mode, small-signal code is utilized to derive the oscillation threshold. A nonlinear single-mode particle tracing code [14] is then employed to simulate the performance of the gyro-TWT on the verge of the oscillation threshold. In both the small-signal and particle-tracing runs, outgoing-wave boundary conditions are imposed at both ends with the space charge effects neglected. The transverse field profile is assumed to be that of a uniform waveguide and the longitudinal field profile is self-consistently evaluated. The magnetic field is assumed to be uniform throughout the interaction structure. Since the structure is uniform in radius and has no reflections at both ends, spurious oscillations of this circuit come from only the absolute instabilities. Table I lists a set of reference parameter as the starting point for our study.

III. ABSOLUTE INSTABILITIES IN A HIGH-ORDER-MODE GYRO-TWT

From the dispersion diagram and simulation results, the most likely absolute instabilities for the modeled gyro-TWT are identified to be the TE_{11} ($s = 1$), TE_{01} ($s = 1$), TE_{21} ($s = 1$), and TE_{02} ($s = 2$) modes (Fig. 2). As shown in Fig. 3, field profiles of these absolute instabilities depend on the sign and magnitude of the k_z value at the intersection point between the beam lines and waveguide modes [24]. These profiles suggest that the high-order and low-k_z modes [Figs. 3(a)-(c)], which are confined to the copper section, can be stabilized with a shortened

copper section, while the high-k_z and lowest-order TE$_{11}$ ($s = 1$) mode [Fig. 3(d)], which penetrates deep into the lossy section, can only be stabilized with heavy wall losses in the lossy section.

Figure 4 displays the parametric dependence of the start-oscillation current (I_{st}) for the four absolute instabilities. Only one of the reference parameter in Table I is varied at a time. It is seen that the TE$_{11}$ mode is sensitive to the wall resistivity and the axial velocity spread, but it depends weakly on the length of the copper section (L_2) due to its deep penetration into the lossy section. In contrast, I_{st} of the remaining modes, which are confined to copper section, show much greater sensitivity to L_2 and are almost unaffected by the wall resistivity, velocity spread, or lossy section length (L_1). In general, power, gain, efficiency, and bandwidth optimizations all require a high operating current. Thus, enhancement of I_{st} for all the oscillating modes, in particular the most persistent TE$_{11}$ mode, becomes the key design consideration.

The discussion above suggests the following procedure for the design optimization. For each set of parameters, we first raise I_{st} of the TE$_{11}$ mode ($I_{st,11}$) to an acceptable value with sufficient wall losses, and then shorten the copper section length (L_2) to stabilize all the remaining absolute instabilities at the value of $I_{st,11}$ just obtained. $I_{st,11}$ and L_2 are then input into the particle-tracing code to simulate the saturated performance. This is a much involved process because several additional parameters, such as the velocity ratio, magnetic field, and lossy section length are all to be varied. The purpose here is not to find the absolute optimum performance in the multi-dimensional parameter space. Nor would such an optimum make much sense because one of more of its parameters is bound to be entirely unrealistic. Rather, some parameters are fixed at reasonable values, while some others are being optimized (again within a reasonable range). The desired design may then be sought out through a tradeoff in regimes of near optimum performance. This is done in the subsequent section.

IV. PERFORMANCES AND TRADEOFFS

We begin by considering the tradeoffs between the (saturated) output power and bandwidth at different values of the applied magnetic field (B_z), expressed in terms of the grazing magnetic field of the operating mode (B_{zg01}). All data points shown here and subsequently are taken just below the threshold of the first absolute instability. As indicated in Fig. 5(a), higher B_z leads to higher output power and narrower bandwidth, while lower B_z results in the opposite. Figure 5(b) plots the bandwidth versus output power at different values of the velocity ratio α ($= v_\perp/v_z$). Given the output power, the corresponding B_z can be read from Fig. 5(a). This figure illustrates the tradeoffs between bandwidth and output power during the magnetic field tuning. Figure 5(b) indicates that electron beams with a lower α are more suitable for high power and wideband operations.

To examine the effect of α upon the performance of the gyro-TWT, it is useful to introduce the power-bandwidth product for each value of α. A large power-bandwidth product means higher output power for the same bandwidth or broader bandwidth for the same output power, since curves for different α in Fig. 5(b) never intersect in the region of interest. Figure 6(a) illustrates the tradeoffs between the maximum achievable power-bandwidth product and efficiency as a function of α. It is worth noting that the decrease in efficiency in the high α region comes from the design goal of a maximum power-bandwidth product. That is, the B_z value for the maximum efficiency operation departs significantly from that for the broadband and high-power operation. Figures 6(a) confirms again that electron beams with a lower α are more suitable for high-power and broadband designs. The interaction efficiency instead of the power-bandwidth product for each value of α is optimized in the same manner as in Fig. 6(a) with the result shown in Fig. 6(b), which demonstrates that electron beams with a higher α are more desirable for high efficiency operation, as is often important for portable systems.

Since the energy exchange in gyro-devices is mainly through the electron azimuthal motion, beam-wave coupling is stronger at higher α values, which leads to higher interaction efficiency. However, stronger coupling also lowers the I_{st} of the associated absolute instabilities, and hence reduces the operating current, interaction efficiency, and output power. Physically, both B_z and α alter the beam-wave resonance conditions [Eq. (1)] for the operating mode as well as for the absolute instabilities. Figures 5 and 6 exhibit the tradeoff between the power-bandwidth product and efficiency. A proper set of B_z and α values can be determined from the tradeoff results according to the design goal.

Figure 7 displays the power and bandwidth as functions of the wall resistivity of the lossy section. As indicated in Fig. 4(b), $I_{st,11}$ increases with an increasing wall resistivity. Higher operating current then leads to higher output power with a slightly increased bandwidth. In practice, maximum output power will be restricted by the maximum achievable wall resistivity, heat dissipation, and current density of cathodes. In particular, heat dissipation is an important issue for CW or long-pulsed operations.

Figure 8 displays the output power, efficiency, and bandwidth as functions of $\Delta v_z/v_z$. The stabilizing effect of $\Delta v_z/v_z$ on the absolute instability is amplified by the k_z value, as can be seen from Eq. (1). As a consequence, $I_{st,11}$ increases sharply with an increasing $\Delta v_z/v_z$. Thus, in essence, a larger $\Delta v_z/v_z$ allows a higher operating current and hence a higher output power. This effect can be exploited only to the extent that the required beam current remains reasonable. By contrast, had the operating current been kept at the same value (rather than the marginally stable value as in Fig. 8), both the output power and efficiency would decrease monotonically with an increasing velocity spread. A closer examination shows that, in the small $\Delta v_z/v_z$ region, only the

high frequency (or k_z) edge is affected, where the efficiency increases and bandwidth is reduced with an increasing $\Delta v_z/v_z$. However, in the large $\Delta v_z/v_z$ region, the efficiency is degraded by $\Delta v_z/v_z$, although the output power continues to increase. The compensating effects of a greater operating current for a higher velocity spread result in a slight increase in bandwidth in the large $\Delta v_z/v_z$ region.

Finally, the dependence of gain and power on the lossy section length (L_l) is considered. The lossy section works as the linear interaction stage for electrons. Hence, a longer lossy section will lead to higher gain of the gyro-TWT. Figure 9 displays the output power and gain as functions of L_l. It is a significant advantage that high gain can always be accomplished by a lengthened L_l, with a minimum effect on the bandwidth and a moderate reduction in output power and efficiency.

Some general trends can be summarized from the results in Figs. 5-9: (1) Large-k_z absolute instabilities, which are insensitive to wall losses, constitute the most severe limitation to the device performance. For the present case, the TE$_{11}$ mode falls into this category; (2) Once the device is stabilized against all absolute instabilities, it is always possible to achieve an ultra high gain by means of a sufficiently long lossy section. This is because an added lossy section to a stable design increases the gain of the operating mode, but it hardly changes the oscillation thresholds; (3) A compromise must be made between the efficiency and power/bandwidth through the choice of the beam α value. A lower α beam allows a higher operating current. This results in higher output power and broader bandwidth. A higher α beam has more free energy for the power conversion, hence it yields a higher efficiency; and (4) Contrary to intuition, a reasonably large velocity spread is conductive to high output power because it brings up the oscillation threshold of the TE$_{11}$ mode and hence the operating current.

For a quantitative illustration, Table II lists three design examples under different design considerations, all with high gain (~70 dB) and each featuring a desirable property such as high power, high efficiency, and wide bandwidth. These examples, with realizable parameters, demonstrate the theoretical viability of a high-performance TE$_{01}$ mode gyro-TWT. Indeed a recent TE$_{01}$-mode gyro-TWT experiment at UC Davis has already demonstrated a record performance at 94 GHz, producing 59-kW saturated output power at 42-dB gain, 26.6% efficiency, and 1.3% bandwidth [18]. With the new insights, it is expected that there is still much room for improvement over the achieved performance. The same trends and design methods apply to still higher order modes or for a non-fundamental cyclotron harmonic. However, the process may be much more involved.

V. CONCLUSION

We have investigated the performance characteristics of a high-order-mode, distributed-loss gyro-TWT in a broad parameter space on the basis of the marginal stability criterion. The beam current of the gyro-TWT is mainly constrained by the large-k_z, TE_{11} absolute instability and can be raised with heavy wall resistivity at the expense of increased wall heating. The low-k_z absolute instabilities may be suppressed with a shortened copper section. Simulation results show a long lossy section can always be employed for ultra high gain, with a minimum effect on the bandwidth and a moderate reduction in output power and efficiency. A low-α beam is preferable for high power and broadband designs, while a high-α beam is suitable for high efficiency operation. In summary, the parametric dependence and design tradeoffs presented in this study provide a useful design guideline for stably operated gyro-TWTs aimed at a specific design goal, as is illustrated in Table II.

Acknowledgements

References

1. V. L. Granatstein, B. Levush, B. G. Danly, and R. K. Parker, IEEE Trans. Plasma Sci. **25,** 1322 (1997).

2. S. H. Gold and G. S. Nusinovich, Rev. Sci. Instrum. **68**, 3945 (1997).

3. K. L. Felch, B. G. Danly, H. R. Jory, K. E. Kreischer, W. Lawson, B. Levush, and R. J. Temkin, Proc. IEEE **87**, 752, (1999).

4. V. L. Granatstein, G. S. Nusinovich, M. Blank, K. Felch, R. M. Gilgenbach, H. Guo, H. Jory, N. C. Luhmann, D. B. McDermott, J. M. Rogers, and T. A. Spencer, in *High-Power Microwave Sources and Technologies*, edited by R. J. Barker and E. Schamiloglu (IEEE, New York, 2001), p. 156.

5. K. R. Chu, Rev. Mod. Phys. **76,** 489 (2004).

6. G. S. Nusinovich, *"Introduction to the Physics of Gyrotrons"* (John Hopkins University Press, Maryland, 2004).

7. M. Blank, B. G. Danly, B. Levush, P. E. Latham, and D. E. Pershing, Phys. Rev. Lett. **79,** 4485 (1997).

8. B. G. Danly, M. Blank, J. P. Calame, B. Levush, K. T. Nguyen, D. E. Pershing, R. K. Parker, K. L. Felch, B. G. James, P. Borchard, P. Cahalan, T. S. Chu, H. R. Jory, T. A. Hargreaves, R. B. True, W. G. Lawson, and T. M. Antenson, IEEE Trans. Plasma Sci. **28**, 713 (2000).

9. M. Blank, K. Felch, B. G. James, P. Borchard, P. Cahalan, T. S. Chu, H. Jory, B. G. Danly, B. Levush, J. P. Calame, K. T. Nguyen, and D. E. Pershing, IEEE Trans. Plasma Sci. **30,** 865 (2002).

10. G. J. Linde, M. T. Ngo, B. G. Danly, W. J. Cheung, and V. Gregers-Hansen, IEEE Trans. Aerosp. Electron. Syst. **44,** 1102 (2008).

11. H. Guo, S. H. Chen, V. L. Granatstein, J. Rogers, G. S. Nusinovich, M. Waters, B. Levush, and W. J. Chen, Phys. Rev. Lett. **79**, 515 (1997).

12. K. R. Chu, H. Y. Chen, C. L. Hung, T. H. Chang, L. R. Barnett, S. H. Chen, and T. T. Yang, Phys. Rev. Lett. **81**, 4760 (1998).

13. G. G. Denisov, V. L. Bratman, A. W. Gross, W. He, A. D. R. Phelps, K. Ronald, S. V. Samsonov, and C. G. Whyte, Phys. Rev. Lett. **81**, 5680 (1998).

14. K. R. Chu, H. Y. Chen, C. L. Hung, T. H. Chang, L. R. Barnett, S. H. Chen, T. T. Yang, and D. Dialetis, IEEE Trans. Plasma. Sci. **27,** 391 (1999).

15. V. L. Bratman, A. W. Gross, G. G. Denisov, W. He, A. D. R. Phelps, K. Ronald, S. V. Samsonov, C. G. Whyte, and A. R. Young, Phys. Rev. Lett. **84,** 2746 (2000).

16. M. Garven, J. P. Calame, B. G. Danly, K. T. Nguyen, B. Levush, F. N. Wood, and D. E. Pershing, IEEE Trans. Plasma Sci. **30**, 885 (2002).

17. J. R. Sirigiri, M. A. Shapiro, and R. J. Temkin, Phys. Rev. Lett. **90**, 258302 (2003).

18. H. H. Song, D. B. McDermott, Y. Hirata, L. R. Barnett, C. W. Domier, H. L. Hsu, T. H. Chang, W. C.Tsai, K. R. Chu, and N. C. Luhmann, Jr., Phys. Plasmas **11**, 2935 (2004).

19. M. Blank, K. Felch, B. G. James, P. Borchard, P. Cahalan, T. S. Chu, H. Jory, B. G. Danly, B. Levush, J. P. Calame, K. T. Nguyen, and D. E. Pershing, IEEE Trans. Plasma Sci. **30**, 865 (2002).

20. M. Blank, P. Borchard, S. Caufman, and K. Felch, in *Proceedings of the IEEE International Vacuum Electronics Conference* (IEEE, New York, 2006), p. 459.

21. M. A. Kempkens, T. J. Hawkey, M. P. J. Gaudreau, and R. A. Phillips, "W-Band transmitter upgrade for the Haystack Ultra Wideband Satellite Imaging Radar (HUSIR)," in *Proceedings of the IEEE International Vacuum Electronics Conference* (IEEE, New York, 2006), p. 551.

22. S. H. Chen, T. H. Chang, K. F. Pao, C. T. Fan, and K. R. Chu, Phys. Rev. Lett. **89**, 268303 (2002).

23. L.R. Barnett, L.H. Chang, H.Y. Chen, K.R. Chu, W.K. Lau and C.C. Tu, Phys. Rev. Lett. **63**, 1062 (1989).

24. W. C. Tsai, T. H. Chang, N.C. Chen, K.R. Chu, H.H. Song, and N.C. Luhmann, Jr., Phys. Rev. E **70,** 056402 (2004).

25. T. M. Antonsen, Jr., S. Y. Cai, and G. S. Nusinovich, Phys. Fluids **B4**, 4131 (1992).

26. T. H. Chang and S. H. Chen, Phys. Plasmas **12**, 013104 (2005).

TABLE I. Reference parameters

Operating mode	TE_{01}
Cyclotron harmonic	fundamental
Waveguide radius (r_w)	0.201 cm
Cutoff frequency	91.0 GHz
Beam voltage (V_b)	100 kV
Velocity ratio ($\alpha = v_\perp/v_z$)	0.8
Velocity spread ($\Delta v_z/v_z$)	5 %
Guiding center position (r_c)	0.48 r_w
Applied magnetic field (B_z)	35.1152 kG
B_z/B_{zg}	1.0
Wall resistivity (ρ)	160,000 ρ_{cu}
Lossy section length (L_1)	12.5 cm
Copper section length (L_2)	1.6 cm

TABLE II. Design examples with different desired features. Unspecified parameters are the same as those in Table I.

	High power design	Wide bandwidth design	High efficiency design
α	0.8	0.8	1.4
L_1 (cm)	16	19.4	15
I_b (A)	12.4	11.5	3.0
B_z (kG)	35.47	34.76	36.24
B_z/B_{zg} (of TE_{01} mode)	1.01	0.99	0.984
Output power (kW)	278.2	175.8	124.1
3-dB bandwidth (%)	5.08	7.04	2.73
Saturated efficiency (%)	22.4	15.3	41.2
Saturated gain (dB)	69	68	70
Central frequency (GHz)	92.0	93.6	91.2
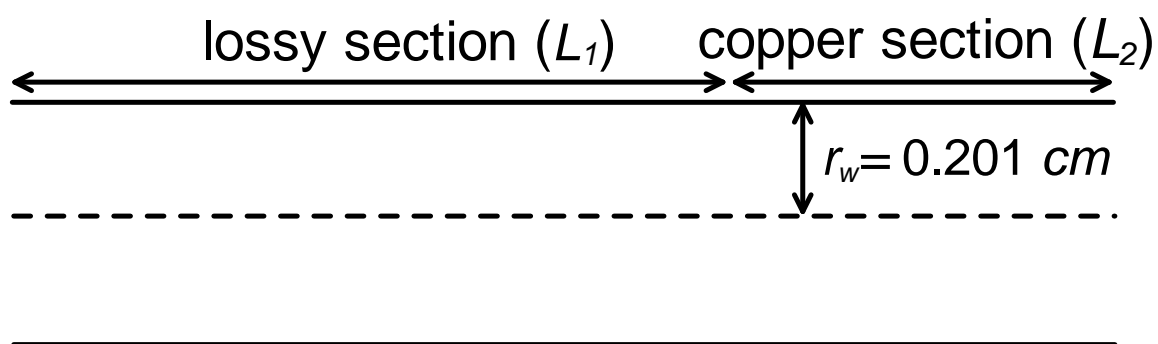
FIG. 1. Configuration of the TE_{01}-mode, 94 GHz gyro-TWT interaction circuit.
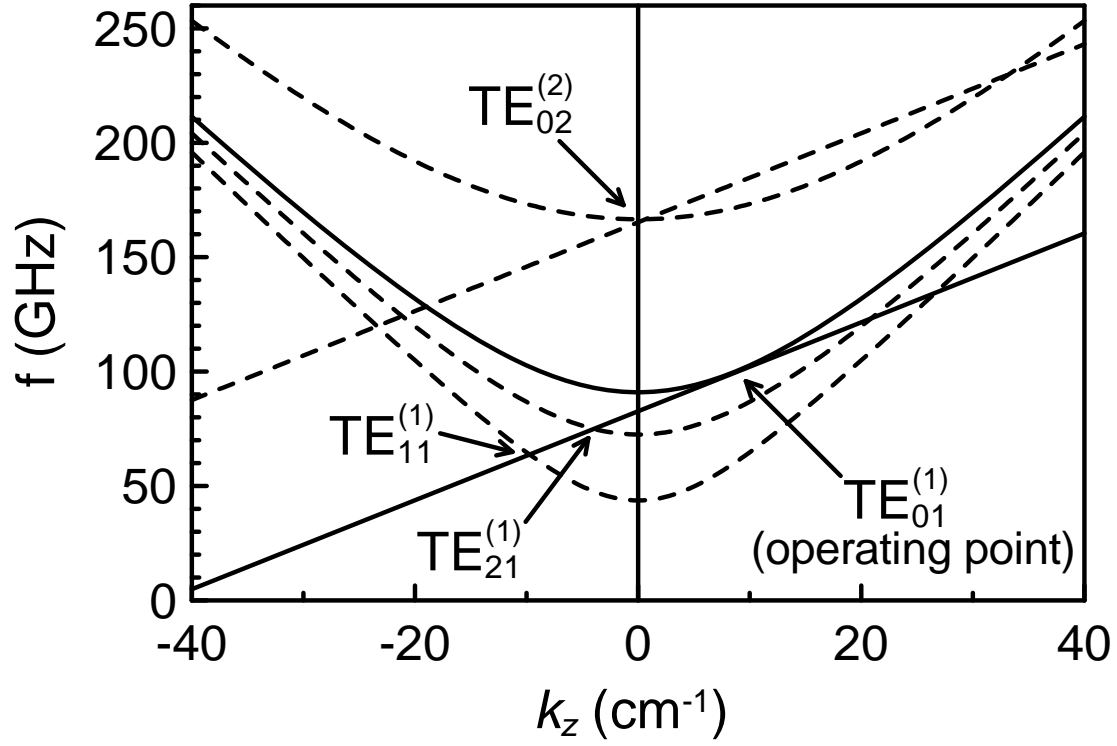
FIG. 2. Frequency versus k_z diagram of the waveguide modes and the beam-wave synchronism lines for a TE_{01}-mode, 94 GHz gyro-TWT operating at the fundamental cyclotron harmonic based on the parameters in Table I.
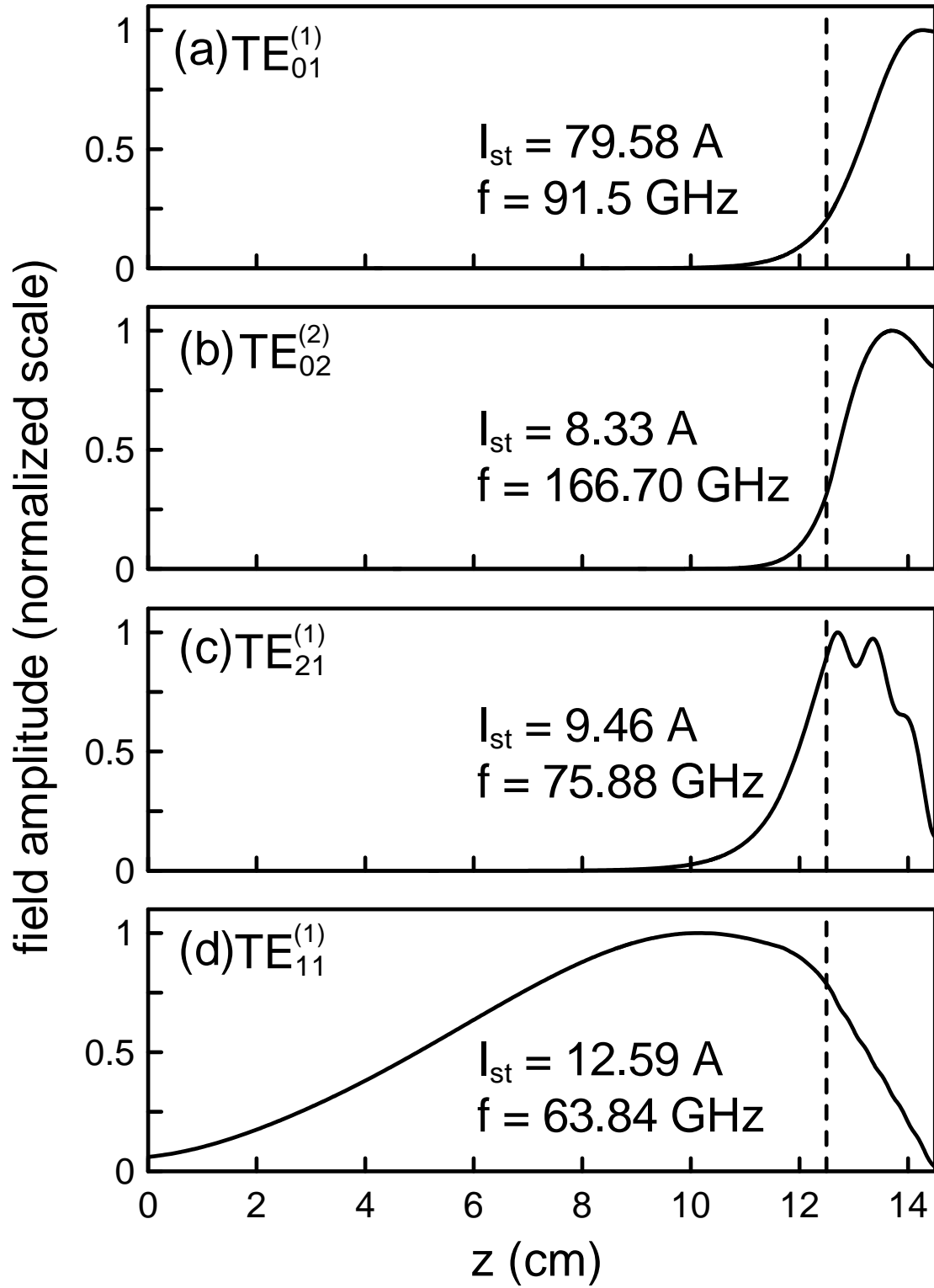
FIG. 3. Field profiles of the four most likely oscillating modes at their respective start-oscillation current. Interface between the lossy and copper sections is indicated by the dashed line. Operating parameters are listed in Table I.
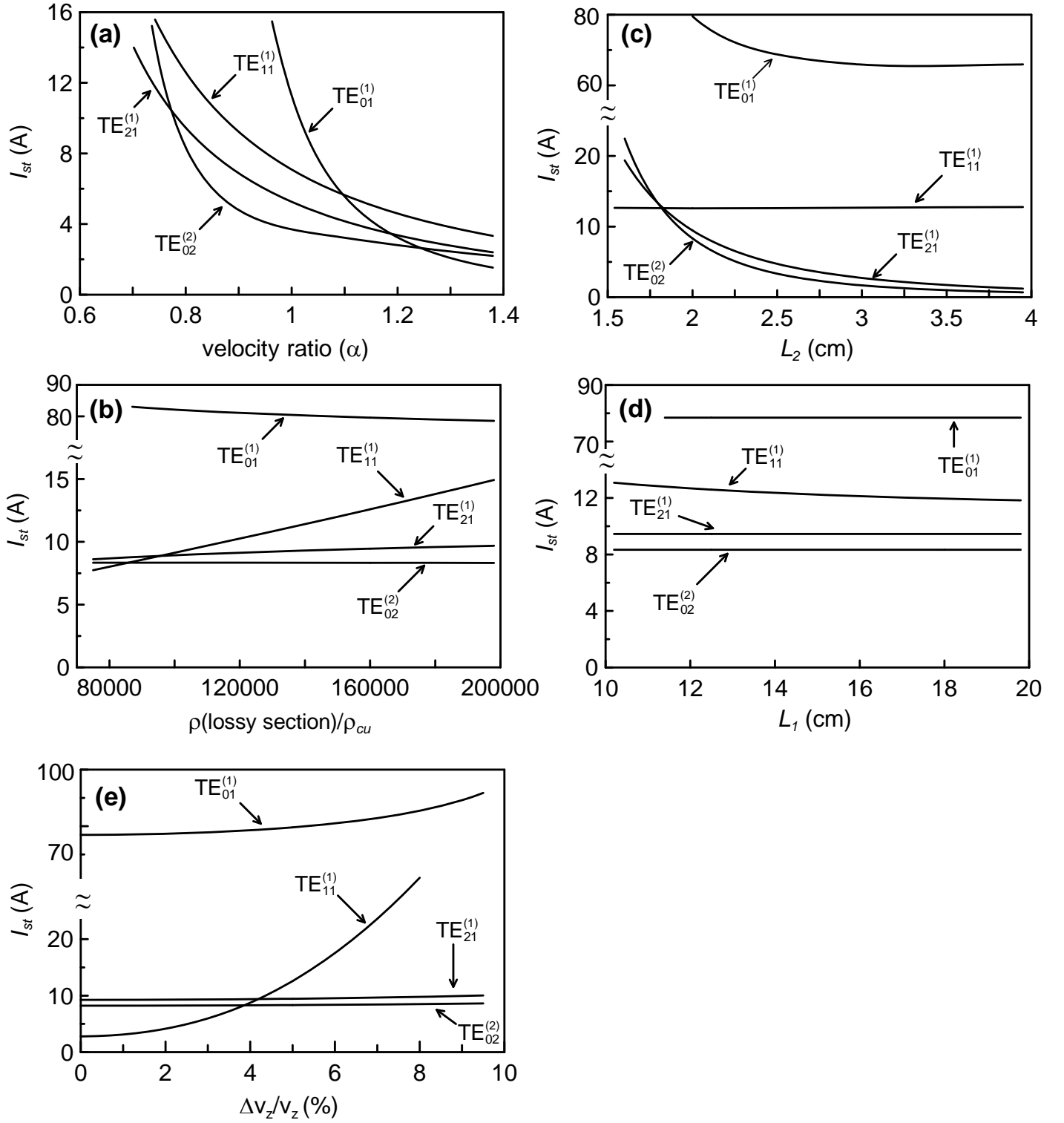
FIG. 4. Parametric dependences of the oscillation thresholds for the four most likely oscillating modes. Operating parameters are listed in Table I. The oscillation thresholds are calculated by varying only one parameter at a time. (a) Start-oscillation currents versus the velocity ratio α. (b) Start-oscillation currents versus the wall resistivity ρ of the lossy section (ρ is normalized to the resistivity of copper ρ_{cu}). (c) Start-oscillation currents versus the copper section length L_2. (d) Start-oscillation currents versus the lossy section length L_1 (e) Start-oscillation currents versus the beam axial velocity spread ($\Delta v_z/v_z$).
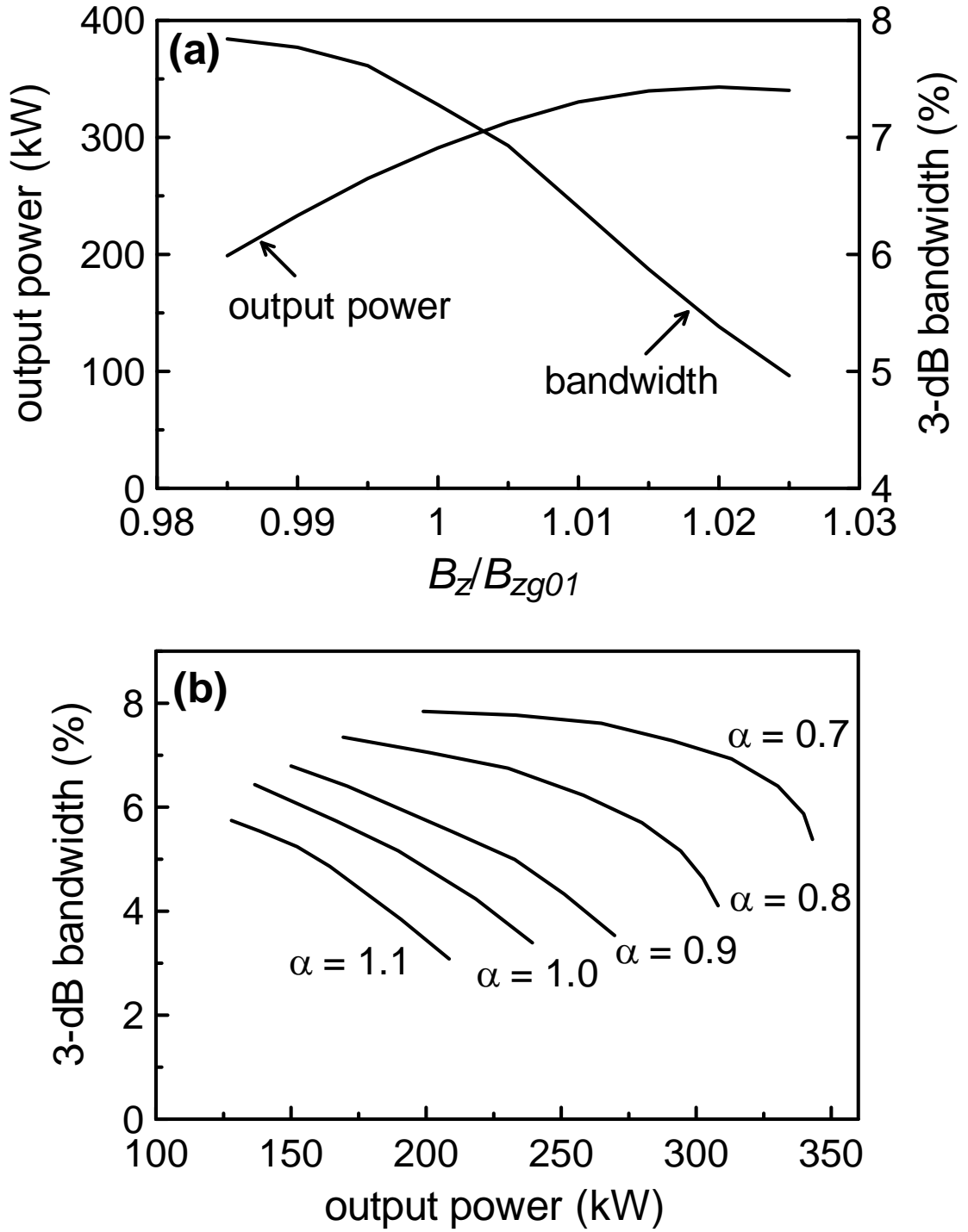
FIG. 5. Performance as functions of magnetic field B_z, showing the tradeoff between power and bandwidth. The magnetic field is normalized to the grazing value (B_{zg01}) for the operating mode. I_b and L_2 are at their marginally stable values. Other parameters, unless specified, are the same as those in Table I. (a) Output power and bandwidth versus B_z (for $\alpha = v_\perp/v_z = 0.7$). (b) Bandwidth versus output power for different values of α.
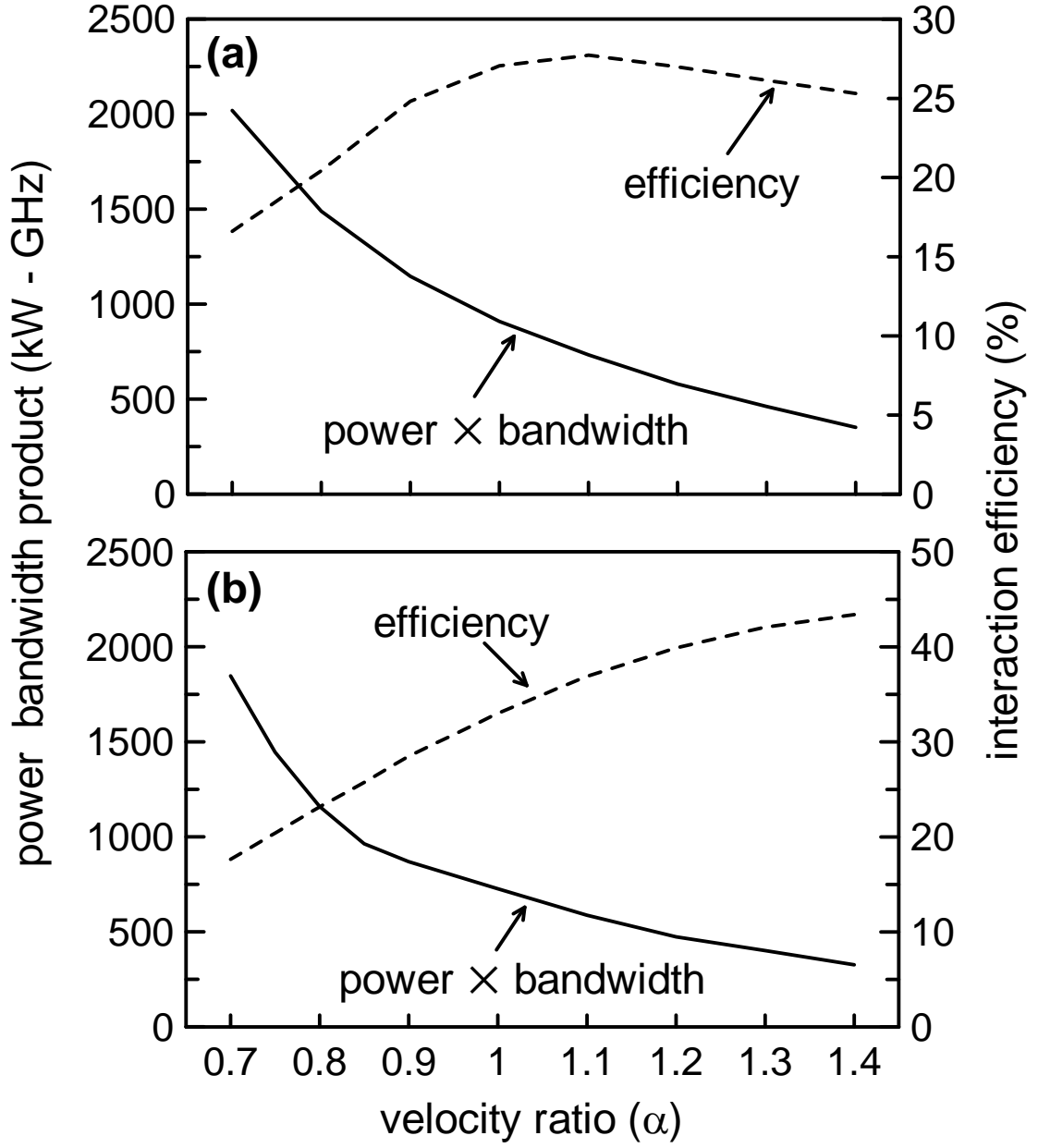
FIG. 6. Power-bandwidth product and efficiency as functions of α. I_b and L_2 are at their marginally stable values and other parameters are the same as in Table I. (a) Power-bandwidth product optimized with respect to I_b and L_2. (b) Efficiency optimized with respect to I_b and L_2.
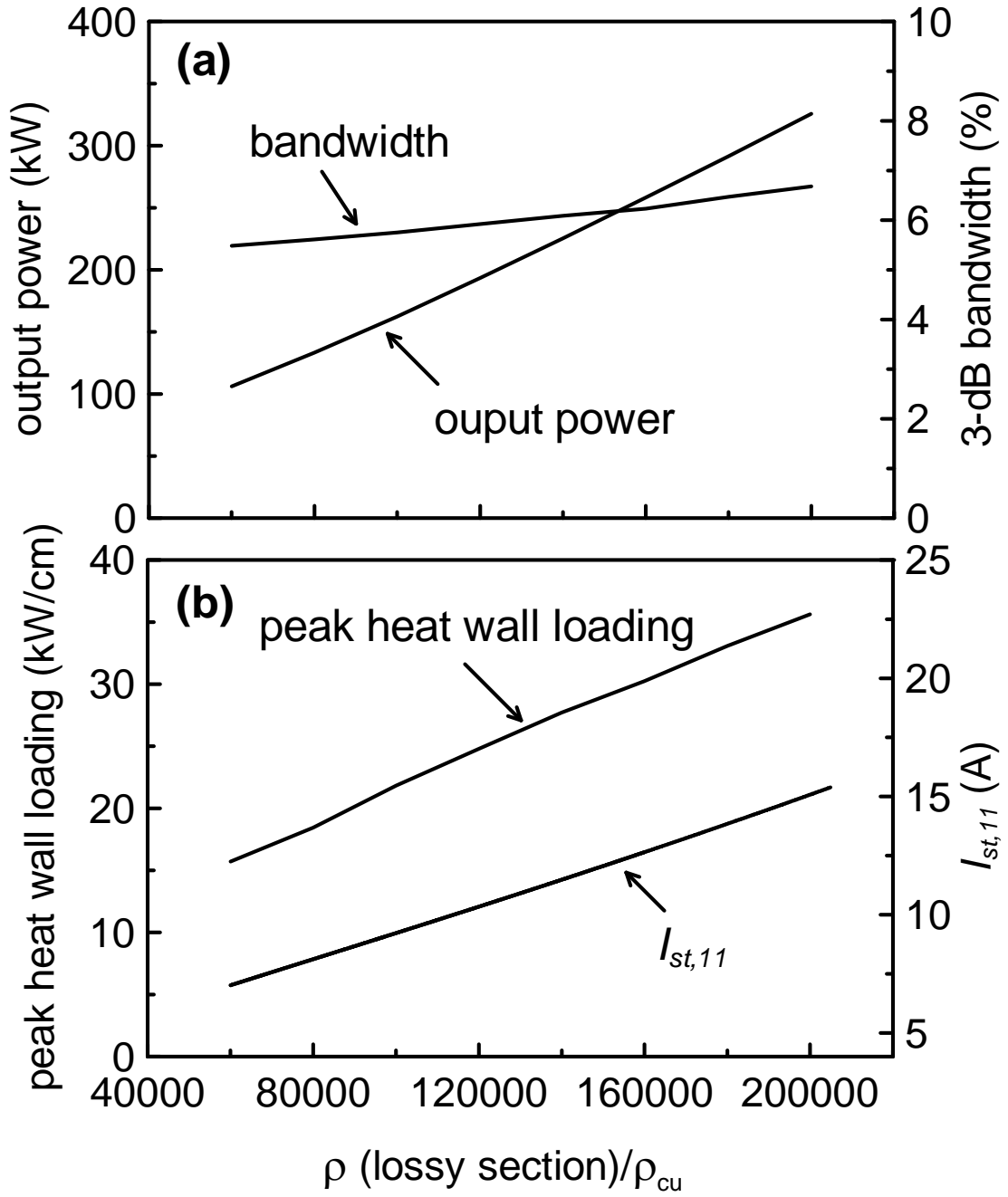
FIG. 7. Performance as functions of the normalized ρ. I_b and L_2 are at their marginally stable values and other parameters are the same as those in Table I. (a) Output power and bandwidth versus ρ. (b) Spatial peak of the wall loading and $I_{st,11}$ versus ρ.
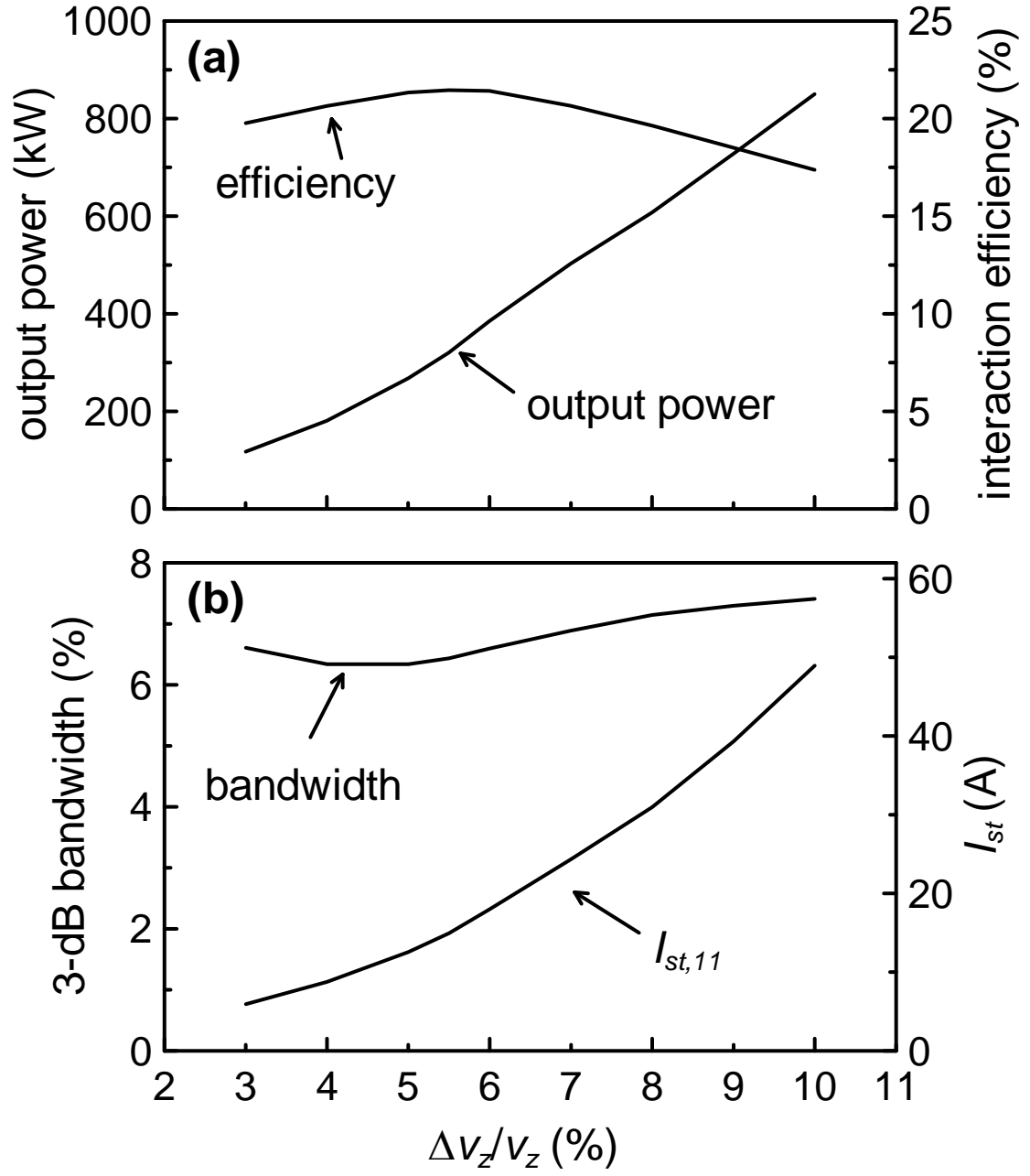
FIG. 8. Performance as functions of $\Delta v_z/v_z$. I_b and L_2 are at their marginally stable values. Other parameters, unless specified, are the same as those in Table I. (a) Output power and efficiency versus $\Delta v_z/v_z$. (b) 3-dB bandwidth and oscillation threshold versus $\Delta v_z/v_z$.
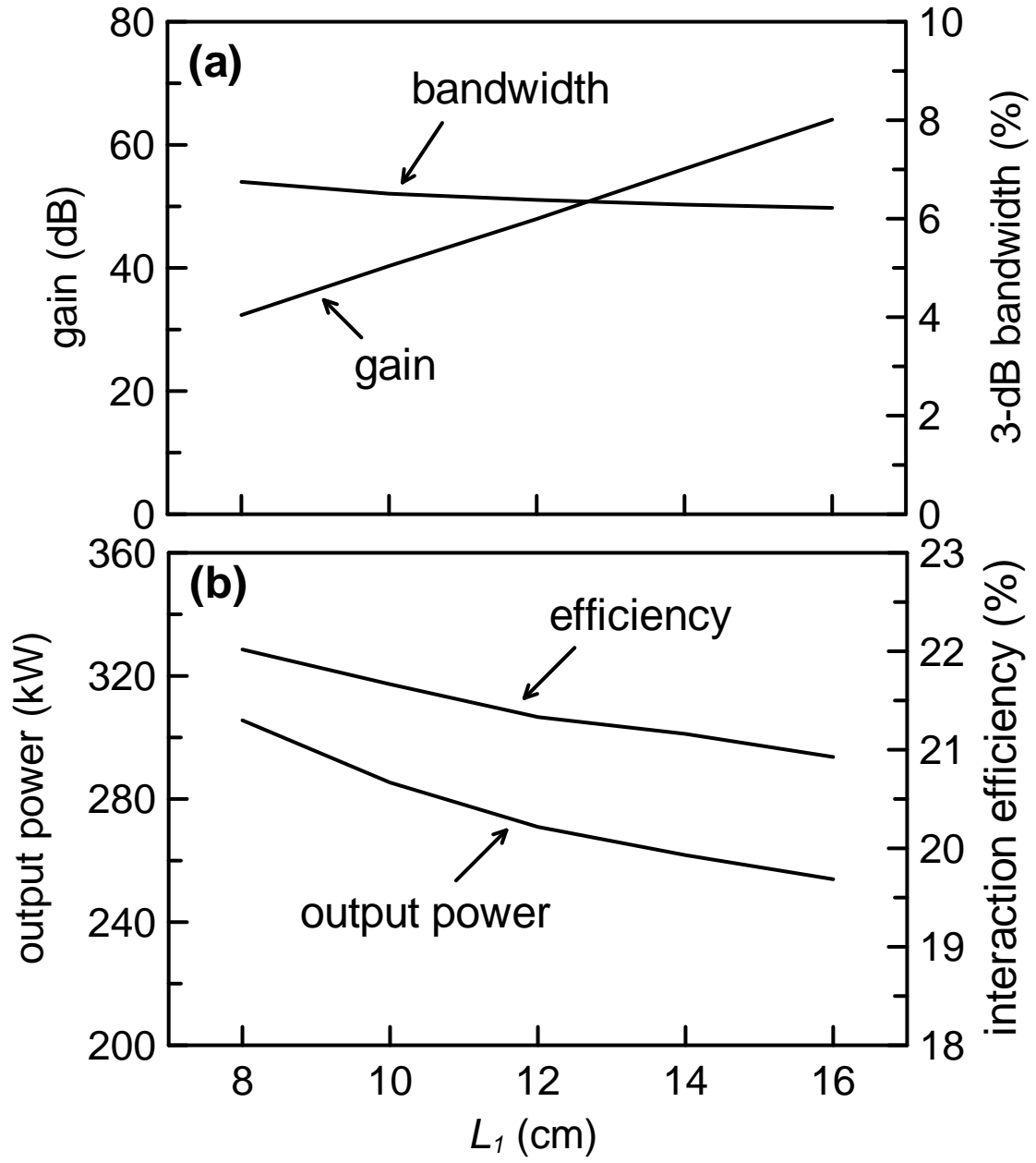
FIG. 9. Performance as functions of the lossy section length L_1. I_b and L_2 are at their marginally stable values and other parameters, unless specified, are the same as those in Table I. (a) Gain and bandwidth versus L_1. (b) Efficiency and output power versus L_1.